# Analysis of Keller Cones for RF Imaging

Anurag Pallaprolu, Belal Korany and Yasamin Mostofi UC Santa Barbara, California, USA, 93106 apallaprolu@ucsb.edu, {belalkorany, ymostofi}@ece.ucsb.edu

Abstract—Imaging still objects with the received signal power of off-the-shelf WiFi transceivers is considerably challenging. The interaction of object edges with the incoming wave, dictated by the Geometrical Theory of Diffraction and the resulting Keller cones, presents new possibilities for imaging with WiFi via edge tracing. In this paper, we are interested in bringing a comprehensive understanding to the impact of several different parameters on the Keller cones and the corresponding edgebased imaging, thereby developing a foundation for a methodical imaging system design. More specifically, we consider the impact of parameters such as curvature of a soft edge, edge orientation, distance to the receiver grid, transmitter location, and other parameters on edge-based WiFi imaging, via both analysis and extensive experimentation. We finally show that Keller cones can be used for imaging objects that lack visibly-sharp edges, as long as the curvature of the edge is small enough, by imaging a number of such daily objects.

## I. INTRODUCTION

There has been a considerable interest in recent years in using WiFi signals for sensing and learning about the environment. WiFi signals, for instance, have been used for localization, tracking, person identification, occupancy analytic, and smart health, among other applications. There has also been work on using WiFi signals for imaging still objects. However, imaging still objects with WiFi signals has been considerably challenging due to the lack of motion (as compared to the aforementioned applications). In fact, work on imaging still objects either focused on using expensive customized mmWave radar equipment [1], or focused on imaging basic scenes with WiFi [2]. Other work has also attempted machine learning for this purpose but with limited generalizability [3].

In a recent work [4], we proposed a different way of thinking about the challenging problem of imaging objects with WiFi, by focusing on how the edges of an object interact with the incoming wave. More specifically, when a wave is incident on an edge, it results in a cone of outgoing rays, dictated by the Keller's Geometrical Theory of Diffraction (GTD) [5]. Thus, the scattered WiFi signals off of objects carry much more information about the edges than the surface points, since edges diffract the incoming wave into many directions (i.e., the diffraction cone), while surface points can appear quasi-specular (near mirror-like) at WiFi frequencies.

In [4], we then proposed **Wiffract**, a new approach to imaging still objects by edge tracing, which uses the Keller cones and the corresponding conic sections to infer the edge angles, via building proper projection kernels. This approach produced promising results, considerably better than when attempting to image object surfaces with WiFi, showing its potential for imaging complex objects. The main focus of [4] was to develop the underlying theories and show the

This work was funded in part by ONR award N00014-20-1-2779, in part by NSF award 2215646 and in part by NSF RI award 2008449.

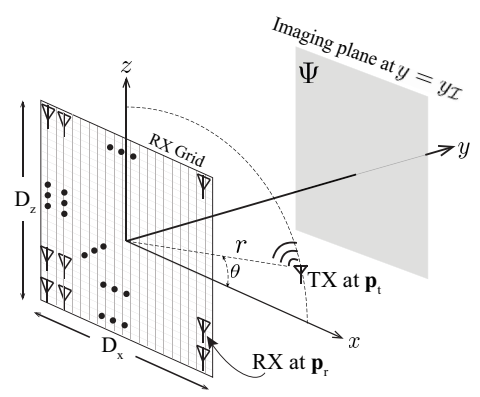


Fig. 1. Imaging setup: a 2D RX grid (at y=0 plane) captures wireless signals emitted by a TX located at  $\mathbf{p}_t = [r\cos\theta, 0, r\sin\theta]$ . The TX illuminates objects in object space  $\Psi$ , a 2D plane parallel to the RX (at  $y=y_{\mathcal{I}}$ ).

performance, mainly for objects with visibly-sharp edges. However, many objects that do not have such sharp edges still have edges with small curvatures. We then have the following question: If the curvature is small enough as compared to the wavelength, can the edge effectively appear as a sharp edge to the incoming wave, producing a similar Keller cone that can be exploited for imaging? Moreover, several other parameters such as edge orientation, distance to the RX grid, TX location, and size of the RX grid affect the exiting Keller cones. In this paper, we then present a comprehensive analysis of the impact of several key parameters on edge-based WiFi imaging, and further support it by extensive experimentation. We finally show the performance of edge-based imaging when imaging daily objects that lack visibly-sharp edges. The analysis and experimentation can provide a foundation for designing edgebased imaging systems, thus motivating future work in this

## II. PROBLEM FORMULATION

Consider an imaging system, shown in Fig. 1. A TX located at  $\mathbf{p}_t = [r\cos\theta, 0, r\sin\theta]$  illuminates the area. The aperture RX is a two dimensional grid of dimensions  $D_x \times D_z$ , located at y=0 plane, composed of uniformly-spaced receiver antennas (indexed by  $\mathbf{p}_r$ ) that capture radiation scattered off of objects in its surroundings. Each antenna is an **off-the-shelf device that can only measure the received signal power** reflected by its surroundings. We are interested in imaging the objects in  $\Psi$ , which is a 2D plane at  $y=y_{\mathcal{I}}$ , parallel to the RX grid. We denote the actual object locations by  $\mathbf{p}_o \in \Theta \subset \Psi$ . Using Born approximation [6], the power of the received signal at  $\mathbf{p}_r$  (after subtracting the direct path from the TX to the RX) can be approximated as follows [4]:

$$P(\mathbf{p}_r) \approx 2\mathcal{R} \left\{ \sum_{\mathbf{p}_o \in \Theta} \Lambda(\mathbf{p}_o, \mathbf{p}_t, \mathbf{p}_r) g^*(\mathbf{p}_t, \mathbf{p}_r) g(\mathbf{p}_o, \mathbf{p}_r) \right\}, \quad (1)$$
where  $\Lambda(\mathbf{p}_o, \mathbf{p}_t, \mathbf{p}_r) = \alpha(\mathbf{p}_t, \mathbf{p}_o) g(\mathbf{p}_t, \mathbf{p}_o) \alpha(\mathbf{p}_o, \mathbf{p}_r) \alpha^*(\mathbf{p}_t, \mathbf{p}_r),$ 

 $\mathcal{R}\{.\}$  is the real part operation,  $g(\mathbf{p}_i, \mathbf{p}_j)$  is the Green's function for the path from  $\mathbf{p}_i$  to  $\mathbf{p}_j$  given by  $e^{-j\frac{2\pi}{\lambda}(||\mathbf{p}_i-\mathbf{p}_j||)}$ ,  $\lambda$  is the wavelength, ||.|| is the norm and  $\alpha(\mathbf{p}_i, \mathbf{p}_j)$  is the corresponding amplitude attenuation factor of the path.

The traditional approach of backward ray-tracing [7] computes the reconstructed image intensity at  $\mathbf{p}_m \in \Psi$  via the following convolution sum over all the RX points

$$\mathcal{I}(\mathbf{p}_m; RX) = \left| \sum_{\mathbf{p}_r \in RX} P(\mathbf{p}_r) g(\mathbf{p}_t, \mathbf{p}_r) g^*(\mathbf{p}_m, \mathbf{p}_r) \right|$$
$$= |\mathcal{I}_S(\mathbf{p}_m) + \mathcal{I}_N(\mathbf{p}_m)|, \tag{2}$$

where  $\mathcal{I}_S(\mathbf{p}_m) = \sum_{\mathbf{p}_r \in RX} \Lambda(\mathbf{p}_m, \mathbf{p}_t, \mathbf{p}_r)$  contains information about the presence of an object at  $\mathbf{p}_m$ , while  $\mathcal{I}_N(\mathbf{p}_m) = \sum_{\mathbf{p}_{o'} \in \Theta} \Lambda(\mathbf{p}_{o'}, \mathbf{p}_t, \mathbf{p}_r) g(\mathbf{p}_{o'}, \mathbf{p}_r) g^*(\mathbf{p}_m, \mathbf{p}_r)$  is an interference term from objects elsewhere [4].

**Definition of an RX Group:** Define the RX group for an object at location  $\mathbf{p}_m$ ,  $RX_{\mathbf{p}_m} \subset RX$ , as the set of all the receiver antennas that capture the radiation scattered off of an object placed at  $\mathbf{p}_m$ .

Problem of Surface Specularity at Lower Frequencies: An underlying assumption for successful imaging via Eq. 2 is that each object point within the imaging plane can scatter the transmitted signal to the whole RX grid (i.e., has a large RX group). In order for a point  $\mathbf{p}_m$  on the object's surface to reflect the incident signal to several of the antenna array elements, the surface at  $\mathbf{p}_m$  needs to appear diffuse (i.e., rough) to the incoming wave. While this is true at very high frequencies (such as mmWave), at lower frequencies (such as WiFi) the perturbations on the surface of an object are typically small when compared to the wavelength. As such, the same surface can appear much smoother and specular to the incoming wave [1]. [1] has also established that many everyday surfaces can appear near-specular (i.e. almost mirror-like) to WiFi signals. This then would result in a very small RX group for a surface point  $(|RX_{\mathbf{p}_m}| \ll |RX|, |.|$  denoting size of set). Thus, relying on imaging surfaces via Eq. 2 at WiFi frequencies will result in poor performance, as shown in the literature [4].

Edges of an object, on the other hand, interact differently with the incoming wave. More specifically, when a wave is incident on an edge point, a cone of outgoing rays emerges according to the Keller's Geometrical Theory of Diffraction (GTD) [5]. This has then become the basis for a new WiFibased imaging method, via edge tracing, that we proposed in a recent work [4]. We next briefly summarize Keller cones and how they can be exploited for tracing edges. This then lays the foundation for the rest of the paper, which is on understanding the impact of many different parameters on such an imaging system via both analysis and experimental validations.

## III. KELLER CONES: THE INTERACTION OF WIRELESS SIGNALS WITH EDGES

Define an edge point as a point on an object where the direction of the surface normal has a discontinuity. We denote the set of edge points by  $\mathcal{E} \in \Theta$ , while all non-edge points are indicated by  $\mathcal{M} = \Theta - \mathcal{E}$ . The Geometrical Theory of Diffraction (GTD) [5], [8] describes the interaction of an

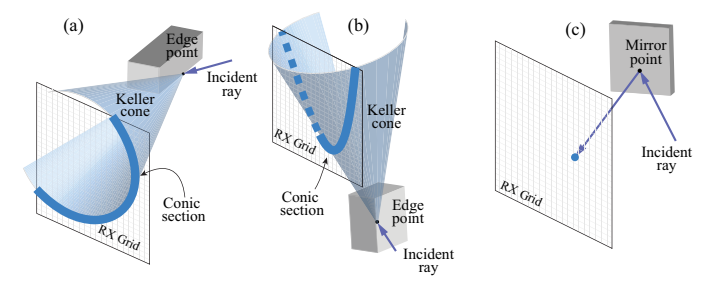


Fig. 2. (a)-(b) Diffracted waves (Keller cones) off of edges with different orientations, which intersect the RX grid in a conic section. (c) Reflected waves off of a surface that appears near-specular (mirror like) to the wave.

electromagnetic wave incident on an edge point from a ray-optics point of view. As shown in Fig. 2 (a)-(b), when a ray is incident on an edge point, the outgoing rays form a cone, known as the Keller cone, with the edge as its axis and the cone angle equal to the angle made by the incident ray with the unit vector along the edge. For a point  $\epsilon \in \mathcal{E}$ ,  $RX_{\epsilon}$  is subsequently given by the intersection of the Keller cone with the RX grid, which is technically known as a conic section, whose structure is dependent on the location of the edge point and the orientation of the edge. On the other hand, a point  $\mu \in \mathcal{M}$  will act near specular at WiFi frequencies, as shown in Fig. 2 (c), resulting in a much smaller RX group  $(|RX_{\mu}| << |RX_{\epsilon}|)$ . See [5], [4] for more details on GTD and Keller cones, as well as other examples of conic sections.

**Edge Imaging with Wiffract:** In recent work [4], we proposed Wiffract, a WiFi-based imaging system that exploits GTD and the resulting Keller cones to image the edges of the objects, using only received power measurements of Eq. 1. We here briefly summarize this approach, which then lays the foundation for our analysis of the next sections. Readers are referred to [4] for more details.

Interaction of the incoming waves with the edges not only results in a bigger RX group, but also allows us to infer the edge orientation, creating the possibility of tracing the edges, as we show next. Let hypothesis  $\mathcal{H}_{\phi_i,\mathbf{p}_m}$  denote the existence of an edge at  $\mathbf{p}_m$  making an angle  $\phi_i$  with the +ve x-axis. Let  $\phi_i \in \Phi$ , which is a discrete set of uniformly-distributed edge orientations in  $[0,\pi)$ . We then define  $RX_{\mathbf{p}_m}(\phi_i)$  as the RX group resulting from the Keller conic section corresponding to the edge orientation hypothesis  $\mathcal{H}_{\phi_i,\mathbf{p}_m}$ . We then have the following edge image for  $\mathbf{p}_m$ , under hypothesis  $\mathcal{H}_{\phi_i,\mathbf{p}_m}$ :

$$\mathcal{I}(\mathbf{p}_m, \mathcal{H}_{\phi_i, \mathbf{p}_m}) = \bigg| \sum_{\mathbf{p}_r \in RX_{\mathbf{p}_m}(\phi_i)} P(\mathbf{p}_r) g(\mathbf{p}_t, \mathbf{p}_r) g^*(\mathbf{p}_m, \mathbf{p}_r) \bigg|.$$

In other words, we perform the convolution only over the RX points that carry the information about the edge hypothesis  $\phi_i$ , which effectively captures the signal term  $|\mathcal{I}_S|$ , while rejecting the interference from the rest of the RX grid. We then select the hypothesis that yields the largest reconstructed intensity  $\mathcal{I}(\mathbf{p}_m; \mathcal{H}_{\phi^*, \mathbf{p}_m})$  and set this as the algorithm's confidence of the presence of an edge with orientation  $\phi^*$  at  $\mathbf{p}_m$  where  $\phi^*(\mathbf{p}_m) = \arg\max_{\phi_i \in \Phi} \mathcal{I}(\mathbf{p}_m, \mathcal{H}_{\phi_i, \mathbf{p}_m})$ .

Once locations with a relatively high confidence of having an edge are identified, their inferred angles are propagated to the rest of the locations using Bayesian information propagation. Due to space constraints, we refer the reader to [4] for more details. In this paper, we are then interested in understanding the impact of several different parameters on the performance of WiFi-based edge tracing. We note that since the analysis/experiments of Sections V and VI are focused on a single edge, we skip the step of belief propagation for these results. We then utilize the full Wiffract pipeline when imaging the objects of Section VII.

### IV. EXPERIMENTAL SETUP

We next describe the technical details of our experimental setup, shown in Fig. 3, before presenting the key results of the paper. We use the onboard antenna ports of two laptops (i.e., 3 antennas per WiFi card of each laptop), to emulate an RX array for imaging. More specifically, the RX grid is synthesized by moving an array of six vertically-oriented omni-directional antennas housed in a wooden carriage. The carriage is horizontally translated with a NEMA 23 belt drive system to scan the x dimension of the grid and vertically translated with an independent NEMA 17 motor to achieve z axis synthesis. We have designed this motorized setup so that the RX grid can be quickly and efficiently generated with only two laptops, with a runtime of 2 minutes to construct a single grid. More specifically, a grid of  $42 \times 98$  receivers is generated by alternating each of the 7 horizontal scans (6 rows per scan), with a vertical separation of 3 cm and a horizontal separation of 1.4 cm. We use off-the-shelf halfspace panel antennas for our WiFi transmitter and log the WiFi CSI (Channel State Information) power measurements off of Intel 5300 NICs of the laptops using the CSI-Tool [9]. For the imaging results demonstrated henceforth, unless otherwise stated, the default dimensions for the RX grid are  $D_x = 1.36$  m and  $D_z = 1.12$  m, the TX location is  $\mathbf{p}_t = [3 \text{ m}, 0, 0], \text{ and } y_{\mathcal{I}} = 1 \text{ m}.$  The imaging plane in all the experiments is  $1.4 \text{ m} \times 1.4 \text{ m}$ , centered around the point  $[0, y_T, 0]$  (See Fig. 1). For all the experimental results, we use background subtraction, as used in [4]. Furthermore, since other work (e.g., [4] and [2]) already established through-wall sensing capabilities of WiFi, in this paper we do not focus on imaging through walls but we note that the results can be extended to through wall imaging.

## V. WHAT CONSTITUTES AN EDGE TO A WAVE?

As discussed in Sec. III, when an electromagnetic wave is incident on a visibly-sharp edge, it generates a Keller cone of diffracted rays. This then raises the following question: If the curvature of an edge is small enough with respect to the wavelength of the incident wave, would it appear as an edge to the wave? A survey of the electromagnetic theory literature indicates that the GTD can be extended to rounded edges [10]. For instance, in [10], it is concluded that an area that does not visually look like a sharp edge can still appear as one to the incoming wave if the radius of its curvature is less than half of the wavelength. This is promising when imaging using edge tracing as it implies that we not only can image objects that have visibly-sharp edges, but can also image a larger category of objects that have edges with small enough

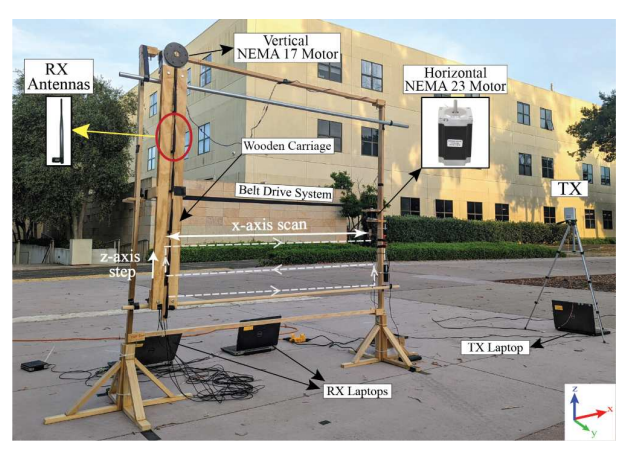


Fig. 3. Experimental setup – WiFi antennas of two laptops are used to emulate an automated 2D RX array, using motors for horizontal and vertical scan.

curvatures. We next show the implication of this for our edgebased imaging system by methodically changing the curvature of an edge, while also using two different wavelengths.

Experimental Validation - Impact of Curvature-Wavelength Relationship on Keller-Cone Based Imaging: Consider an incident wave with wavelength  $\lambda$ , and a rounded edge with a radius of curvature  $r_c$ . We change the radius methodically, from 0 cm (sharp edge) to 6 cm, as shown in Fig. 4 (top row). For each case, we image the edge, using the GTD-based approach of Wiffract as discussed in Sec. III, and the setup of Sec. IV, using WiFi at both 5 GHz and 2.4 GHz. The second row shows the imaging results for 5 GHz (subchannel at 5.32 GHz), for which the theoretically-predicted limit for the soft edge to appear as a sharp one to the wave is 2.8 cm. As can be seen, the edge can be visibly seen in the images up to 3 cm very well. Even for 4 cm, the edge is still well imaged. However, the imaging quality degrades after that as expected. This is consistent with the theories of GTD as the threshold of  $\frac{\lambda}{2}$  is not discussed as a binary threshold but rather as a gradual one where the edge impact is starting to diminish afterwards [10]. The third row then shows the imaging results at 2.4 GHz. We expect to lose resolution when reducing the frequency from 5 GHz, as can be seen from the leftmost figure that images the sharp edge. However, we can see that the imaging results are pretty similar for all the radii from 0 to 6 cm, since they are all below the cutoff of  $\frac{\lambda}{2} = 6.2$  cm. Overall, the results confirm that curvatures with small enough radii, as compared to the wavelength, can also act as sharp edges when interacting with the incoming waves, resulting in Keller cones that can then be exploited for imaging, as is done in Wiffract. In Sec. VII, we show how we can utilize this and image a number of daily objects that do not have sharp edges but have small enough curvatures. In the rest of the paper, we use WiFi at 5GHz for imaging.

### VI. EDGE VISIBILITY ANALYSIS

Several parameters can affect the exiting Keller cone of an edge. Sample important ones include location and orientation of an edge, distance of the edge to the RX grid, location of the transmitter, and size of the RX grid. These parameters determine if the resulting Keller cone intersects with the RX

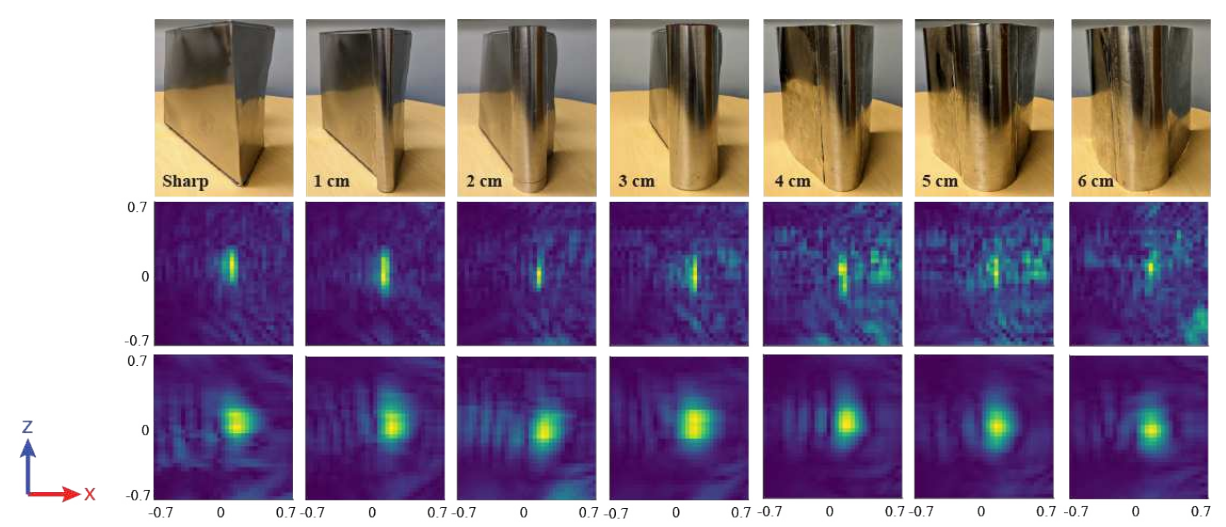


Fig. 4. Experimental Results on the Impact of Curvature: (Top) Edges with different radii of curvature, (middle) Wiffract's edge imaging results with 5 GHz WiFi, and (bottom) Wiffract's edge imaging results with 2.4 GHz WiFi. Quality of edge imaging starts to degrade when the radius of curvature exceeds  $\lambda/2$  (See the color PDF for best viewing).

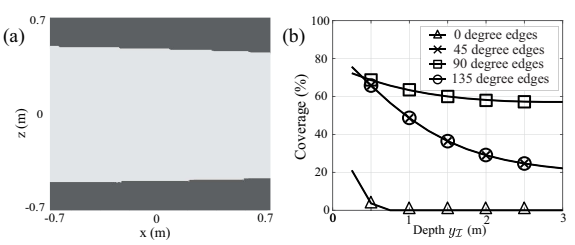


Fig. 5. (a) Visibility (light) and blind (dark) regions for a vertical edge in an imaging plane at  $y_{\mathcal{I}} = 0.6$  m, with a TX at  $\mathbf{p}_t = [3, 0, 0]$ . (b) Impact of depth  $(y_{\mathcal{I}})$  and edge orientation on the coverage, for the same imaging setup.

grid, and if so, the extent of the intersection (i.e., the number of RX antennas affected by it). In this section, we first analyze the impact of these parameters. We then experimentally validate the observations with several experiments. Such a study can then result in clear guidelines when designing the imaging system, as we shall discuss.

We start by defining the *blind* region of  $\Psi$ . We say a location in  $\Psi$  is in a blind region if the resulting Keller cone of an edge at that location does not reach the RX grid. Similarly, the edge is said to be in a region of *visibility* if its exiting Keller cone has a non-zero overlap with the RX grid. We next show the impact of edge orientation, the distance between the RX grid and the imaging plane, the RX grid size, and the TX location on edge visibility.

Fig. 5 (a) shows the visibility region for a vertical edge in  $y_{\mathcal{I}}=0.6~m$ , and with the TX location at  $\mathbf{p}_t=[3~\mathrm{m},0,0]$ . We note that for the analysis of this section, the edge height is 30 cm, small enough so it only occupies a very small number of pixels in the imaging plane. Finally, the grid size is  $D_x=1.36~\mathrm{m}$  and  $D_z=1.12~\mathrm{m}$ , unless stated otherwise. The light gray part of the imaging plane denotes the *visible region*, while the darker region is the *blind* region. As can be seen, the location of the edge can highly affect its visibility. We next define the term *coverage*, as the percentage of the imaging plane that is visible. For instance, in the example of Fig. 5 (a), the coverage is 67.1%. We next use coverage as a metric to show the impact of changing system parameters.

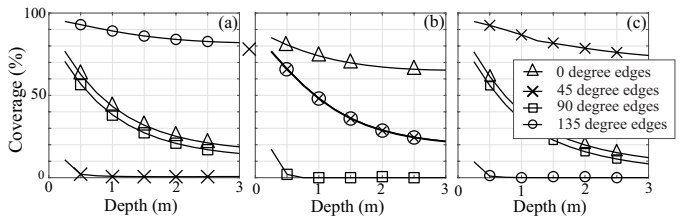


Fig. 6. Coverage as a function of the depth,  $y_{\mathcal{I}}$ , for different TX locations at r=3~m and (a)  $\theta=45^\circ$ , (b)  $\theta=90^\circ$ , and (c)  $\theta=135^\circ$ , and for different edge orientations.

More specifically, Fig. 5 (b) shows the coverage as a function of the depth  $(y_{\mathcal{I}})$ , for different edge orientations, while the rest of the setup stays the same. It can be seen that the coverage decreases as the imaging plane is moved away from the RX grid, as it is more likely for the Keller cone of the edge to miss the grid when the edge is farther away. Moreover, the figure shows that the coverage depends on the orientation of the edge: a TX placed at  $\mathbf{p}_t = [3 \text{ m}, 0, 0]$  illuminates vertical edges the best, while minimally illuminating horizontal edges.

We next move the TX on a semi-circle of radius r = 3 maround the RX, as shown in Fig. 1. Fig. 6 shows the coverage when the TX is placed at angles  $\theta = 45^{\circ}, 90^{\circ}$ , and  $135^{\circ}$  on this semi-circle, as a function of the depth  $y_{\mathcal{I}}$ , and for different edge orientations. It can be seen that different TX locations illuminate the edges of different orientations differently. For instance, the TX at  $\theta = 45^{\circ}$  illuminates the edges of  $135^{\circ}$  the best, with minimal coverage for edges at 45°, and a reasonable coverage for horizonal and vertical edges. On the other hand, the TX at  $\theta = 90^{\circ}$  illuminates the horizontal edges the best, with a minimal coverage for vertical edges, and a reasonable coverage for edges at 45° and 135°. In general, we can see that a TX at an angle  $\theta$  best illuminates edges which make an angle  $\theta + 90^{\circ}$  with the +ve x-axis in the imaging plane. This gives rise to a simple recipe for the number and locations of the needed transmitters, to have a high enough coverage for most-likely edge orientations. For instance, a survey of different objects reveal that most common edges are horizontal and vertical, which suggests that two transmitters at  $\theta = 0^{\circ}$ 

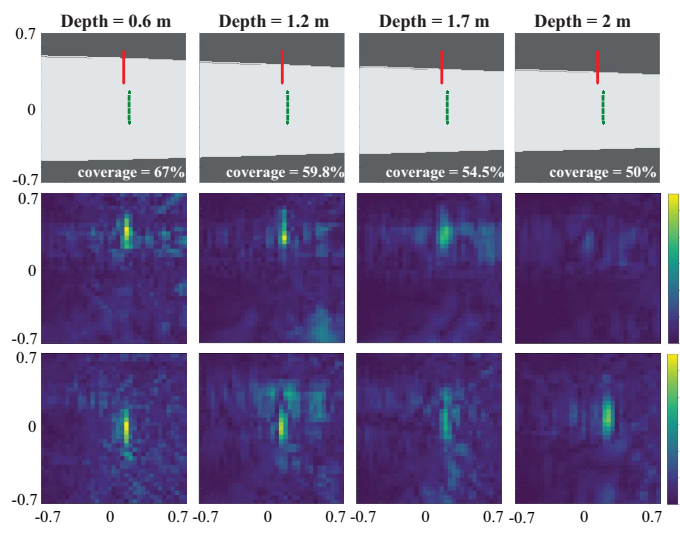


Fig. 7. (Top) Theoretically visible (bright) and blind (dark) regions for different depths, and for two different edge locations. Experimental Validations – (Middle) Wiffract's imaging results when placing the top edge at different depths. Imaging quality degrades as depth increases. (Bottom) Wiffract's imaging results when placing the bottom edge at different depths. The imaged edge remains visible even as depth increases. Experimental results are consistent with the top row analysis (See color PDF for best viewing).

and  $90^{\circ}$  will be important for proper illumination.

**Experimental Validation:** We next experimentally verify the aforementioned analysis by showing the impact of key parameters on edge-based imaging quality.

1) Distance between the edge and the RX grid: Fig. 7 shows the imaging results of a series of experiments in which we place a 30-cm sharp vertical edge at various depths of  $y_{\mathcal{I}} = 0.6, 1.2, 1.7,$  and 2 m, and at two different locations. The top row shows the theoretical visibility regions (bright color) for each distance, as well as the location of the two edges. The middle row then shows the imaging results when placing the edge at the top location. As can be seen, the edge is imaged well when it is closer to the RX grid but the quality degrades as the edge is moved farther away. This is consistent with the top row analysis as the top edge starts to move to the blind region as the distance increases. On the other hand, for the bottom location placement of the edge, the top row indicates that the edge should remain in the visible region even as the distance increases in this case. The Wiffract imaging experiments of the bottom row then confirm this. More specifically, we can see that the edge is imaged well even for farther distances. Note that, due to path loss, placing the edge farther from the grid in general results in a weaker measured diffracted signal, which slightly reduces the intensity of the image.

2) Impact of the RX grid size: Fig. 8 next shows the impact of the RX grid size on the imaging performance for a vertical edge placed at two different locations that are indicated in the top figure. For these results, the depth is fixed at  $y_{\mathcal{I}} = 1$  m and the transmitter is at  $\mathbf{p}_t = [3 \text{ m}, 0, 0]$ . From analysis, we expect the visibility region to shrink as the RX grid gets smaller since there is a higher chance of the Keller cone missing the grid, confirmed by the top row. We can furthermore see that when the edge is at the top location, it ends up in the blind region as the RX grid size shrinks. Finally, even when

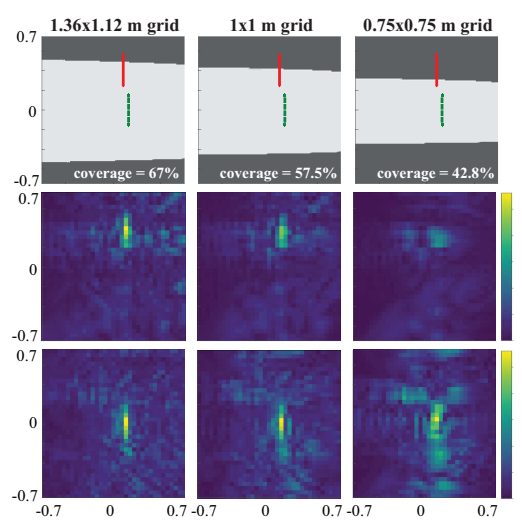


Fig. 8. (Top) Theoretically visible (bright) and blind (dark) regions for different RX grid sizes, and for two different edge locations. Experimental Validations – (Middle) Wiffract's imaging results for the top edge with different RX sizes. Imaging quality degrades for the smaller grid sizes as the edge moves to the blind region. (Bottom) Wiffract's imaging results for the bottom edge with different RX sizes. The imaged edge remains visible for all RX sizes but the quality degrades as the RX size decreases (See color PDF for best viewing).

in the visible region, as the RX grid size shrinks, we expect the imaging quality to degrade since the coverage for each point will be less (less RX points affected by the Keller cone), and the interference term will become higher. The middle row then shows the imaging results when placing the edge at the top location. It can be seen that while the edge is imaged reasonably well for a larger RX grid, the imaging performance degrades as the RX size decreases. The bottom row then shows the imaging results when the vertical edge is at the lower location, which is in the visible region all the time. It can be seen that the imaged edge is visible for all the sizes. However, as the RX size becomes smaller, the imaging quality degrades as the Keller cone affects less RX antennas.

3) Impact of the edge orientation: Fig. 9 shows the imaging results for edges with different orientations  $(0^{\circ}, 45^{\circ}, 90^{\circ}, 135^{\circ})$ , using a fixed RX grid size of 1.36 m  $\times 1.12$  m, depth of  $y_{\mathcal{I}} = 1.5$  m, and TX at  $\mathbf{p}_t = [3 \text{ m}, 0, 0]$ . The top row shows the analysis results, which indicates that this transmitter location best illuminates vertical edges, as discussed earlier. The bottom row then shows the imaging results. As can be seen, the vertical edge is the only one that is imaged, while the Keller cones of the edges at other orientations did not have much overlap with the RX grid, resulting in them not being imaged. Note that the impact of edge orientation also depends on the edge location.

4) Impact of the TX location: Fig. 9 showed the illumination capabilities of a TX placed on the side of the RX grid, i.e. at  $\mathbf{p}_t = [3 \text{ m}, 0, 0]$  ( $\theta = 0^\circ$  in Fig. 1). Fig. 10 next shows the same results, but with the TX located above the RX grid at [0, -1.3 m, 1.2 m] (Due to physical limitations of the imaging setup, this is the closest location to create  $\theta = 90^\circ$  of the theoretical results of Fig. 1). The top row shows that the tested  $0^\circ$ ,  $45^\circ$ , and  $135^\circ$  edges are in the visible region for this TX placement. On the other hand, there is very little coverage

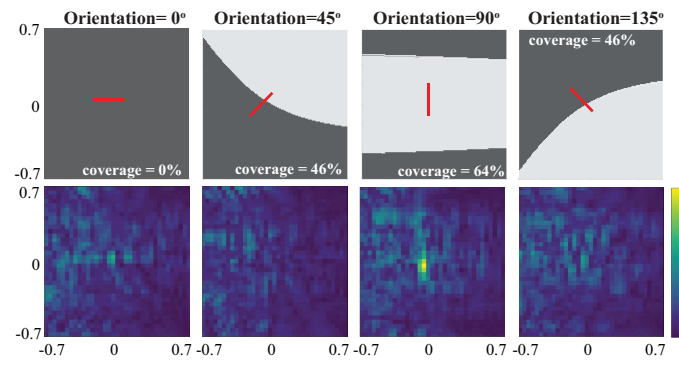


Fig. 9. (Top) Theoretically visible (bright) and blind (dark) regions for different edge orientations, and a TX located at  $\mathbf{p}_t = [3\ m,0,0]$ . (Bottom) Wiffract's imaging results. It can be seen that only the vertical edge is visibly imaged at this location (See color PDF for best viewing).

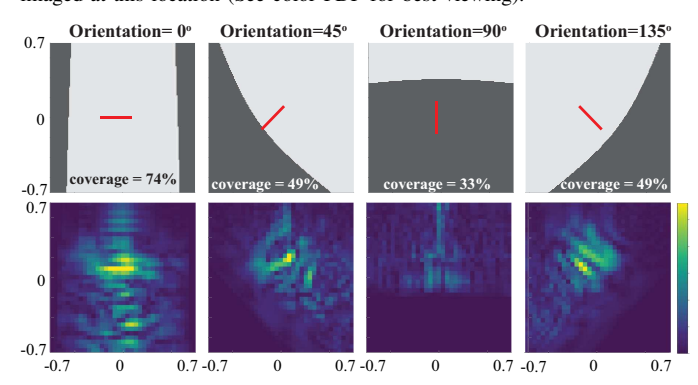


Fig. 10. (Top) Theoretically visible (bright) and blind (dark) regions for different edge orientations, and a TX located at  $\mathbf{p}_t = [0, -1.3 \text{ m}, 1.2 \text{ m}]$ . (Bottom) Wiffract's imaging results. It can be seen that the vertical edge is not imaged while the horizontal edge is imaged the best by this TX location. (See color PDF for best viewing)

when illuminating vertical edges in this case. The second row then shows the experimental results, which confirms that the vertical edge cannot be imaged while the horizontal edge is imaged the best, and the other two orientations are imaged, but with a lesser quality. These results are consistent with the earlier analysis stating that a TX located at an angle  $\theta$  on a semi-circle around the RX grid is best for imaging edges that are at angles  $\theta + 90^{\circ}$ .

### VII. IMAGING OBJECTS WITH DIFFERENT CURVATURES

We next focus on the performance of Wiffract when imaging daily objects that do not necessarily have sharp edges, but have sides with small curvatures. We utilize three transmitters located at  $\mathbf{p}_{t_1} = [3 \text{ m}, 0, 0], \ \mathbf{p}_{t_2} = [0, -1.3 \text{ m}, 1.2 \text{ m}]$  and  $\mathbf{p}_{t_3} = [-3 \text{ m}, 0, 0]$ , for an imaging plane at  $y_{\mathcal{I}} = 1.5 \text{ m}$ . We run the full Wiffract algorithm [4], briefly summarized in Sec. III. More specifically, in addition to the edge hypothesis testing of previous sections, Wiffract fuses the images of 3 transmitters, after thresholding the heat maps, and performs Bayesian information propagation on the fused image, yielding a final edge map. Due to space constraints, we refer the readers to Sec. 4.2 of [4] for more details on the methodology. Note that no machine learning is used for these results. Fig. 11 (Top) shows the objects: a ladder, a chair, a triangle, and a post with a suspended box. As can be seen, these objects do not have sharp edges but the sides have small enough curvatures

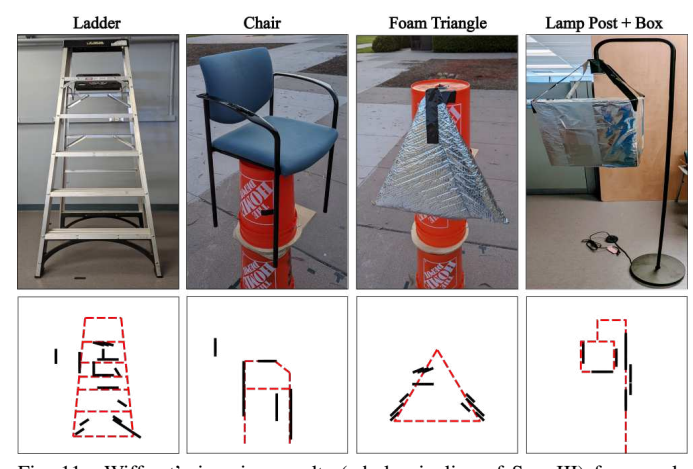


Fig. 11. Wiffract's imaging results (whole pipeline of Sec. III) for sample everyday objects, with a variety of curvatures. As seen, we can image these objects well with only WiFi received power, using fundamentals of how small curvatures interact with incoming waves, and the resulting Keller cones. for this wavelength. The second row then shows the final edge imaging results of Wiffract. As can be seen, Wiffract is able to image the edges of these objects very well, with only WiFi received power measurements. The results further confirm the prior edge illumination analysis of Figs. 9 and 10. To the best of our knowledge, no other approach has produced results of this quality when imaging with only WiFi.

### VIII. CONCLUSION

In this paper, we provided an in-depth analysis of the interaction of wireless signals with object edges and its impact on WiFi-based imaging systems. More specifically, we considered the impact of curvature of a soft edge, edge orientation, distance to the receiver grid, transmitter location, and other parameters on the resulting Keller cones and the corresponding edge-based imaging system, via both analysis and extensive experimentation. We also showed that soft edges with a small enough curvature appear as sharp edges to the wave, and can be similarly imaged using edge tracing via Wiffract, and further imaged a number of such daily objects.

## REFERENCES

- F. Zhang, C. Wu, B. Wang, and K. R. Liu, "mmEye: Super-Resolution Millimeter Wave Imaging," *IEEE Internet of Things Journal*, vol. 8, no. 8, pp. 6995–7008, 2020.
- [2] C. R. Karanam and Y. Mostofi, "3D through-wall imaging with unmanned aerial vehicles using WiFi," in 16th ACM/IEEE IPSN, 2017.
- [3] C. Li et al., "WiFi see it all: generative adversarial network-augmented versatile WiFi imaging," in Proceedings of the Conference on Embedded Networked Sensor Systems, 2020, pp. 436–448.
- [4] A. Pallaprolu, B. Korany, and Y. Mostofi, "Wiffract: A New Foundation for RF Imaging via Edge Tracing," in *Proceedings of the 28th Annual International Conference on Mobile Computing And Networking*, 2022.
- [5] J. B. Keller, "Geometrical theory of diffraction," *Journal of the Optical Society of America*, vol. 52, no. 2, pp. 116–130, 1962.
- [6] W. C. Chew, Waves and fields in inhomogenous media. Wiley, 1995
- [7] D. Huang, R. Nandakumar, and S. Gollakota, "Feasibility and limits of WiFi imaging," in *Proceedings of the 12th ACM Conference on Embedded Network Sensor Systems*, 2014, pp. 266–279.
- [8] R. G. Kouyoumjian and P. H. Pathak, "A uniform geometrical theory of diffraction for an edge in a perfectly conducting surface," *Proceedings* of the IEEE, vol. 62, no. 11, pp. 1448–1461, 1974.
- [9] D. Halperin, W. Hu, A. Sheth, and D. Wetherall, "Tool release: Gathering 802.11n traces with channel state information," ACM SIGCOMM, 2011.
- [10] R. Ross and M. Hamid, "Scattering by a wedge with rounded edge," IEEE Transactions on Antennas and Propagation, vol. 19, 1971.